Geophysical Research Letters

RESEARCH LETTER
10.1029/2021GL093971

Reconciling Human and Natural Drivers of the Tripole Pattern of Multidecadal Summer Temperature Variations Over Eurasia

Wenjian Hua[1], Minhua Qin[1], Aiguo Dai[2], Liming Zhou[2], Haishan Chen[1], and Wanxin Zhang[1]

[1]Key Laboratory of Meteorological Disaster, Ministry of Education (KLME)/Joint International Research Laboratory of Climate and Environment Change (ILCEC)/Collaborative Innovation Center on Forecast and Evaluation of Meteorological Disasters (CIC-FEMD), Nanjing University of Information Science and Technology, Nanjing, China, [2]Department of Atmospheric and Environmental Sciences, University at Albany, State University of New York, Albany, NY, USA

Key Points:

- More than half of the multidecadal surface air temperature (SAT) variations from 1950 to 2014 over Europe-west Asia and East Asia resulted from external forcing
- The forced SAT multidecadal variations over Eurasia are mainly caused by changes in greenhouse gases and aerosols
- Our study helps reconcile human and natural drivers of the tripole pattern of multidecadal summer temperature variations over Eurasia

Supporting Information:

Supporting Information may be found in the online version of this article.

Correspondence to:

M. Qin and A. Dai,
qinminhua@gmail.com;
adai@albany.edu

Citation:

Hua, W., Qin, M., Dai, A., Zhou, L., Chen, H., & Zhang, W. (2021). Reconciling human and natural drivers of the tripole pattern of multidecadal summer temperature variations over Eurasia. *Geophysical Research Letters*, *48*, e2021GL093971. https://doi.org/10.1029/2021GL093971

Received 22 APR 2021
Accepted 30 JUN 2021

Abstract The recent summer surface air temperature (SAT) changes over densely populated Eurasia exhibit a non-uniform pattern with amplified warming over Europe and East Asia (EA) but weak warming over Central Asia (CA), forming a wave train-like structure. However, the key factors that determine this non-uniform warming pattern remain unclear. By analyzing observations and model simulations, here, we show that more than half of the SAT multidecadal variations from 1950 to 2014 over Europe-west Asia and EA may have resulted from external forcing, rather than from internal variability in the Atlantic as previously thought. In contrast, the recent SAT over CA is influenced mainly by internal variations in the Atlantic and Pacific oceans. Large ensemble model simulations suggest that the forced SAT multidecadal variations over Eurasia are mainly caused by changes in greenhouse gases and aerosols. Our findings provide strong evidence for major impacts of external forcing on multidecadal climate variations over Eurasia.

Plain Language Summary Previous studies have documented non-uniform decadal warming rates in summer since the mid-1990s over densely populated Eurasia, with amplified warming over Europe and East Asia (EA) but weak warming over Central Asia. This unique tripole warming pattern and its cause have attracted considerable attention. It may arise from internal variability (IV; e.g., Atlantic Multidecadal Oscillation [AMO]) and/or external forcing. Furthermore, it was found that the recent AMO resulted from both IV and decadal changes in aerosols. Thus, the relative contributions of IV and external forcing to the recent Eurasian warming pattern remain unclear. Here we show that the surface air temperature multidecadal variations since 1950 over Eurasia are caused by both IV and external forcing, with more than half of the variations over Europe-west Asia and EA resulted from external forcing (i.e., greenhouse gases [GHGs] and aerosols), in contrast to the previous notion that the non-uniform warming is mainly originated from the Atlantic Ocean. Looking ahead into the upcoming decades, aerosols will continue to decrease, whereas the AMO will likely be in its positive phase. These changes, together with continued increases in GHGs, will accelerate warming trends over Eurasia and further exacerbate summer heat waves.

1. Introduction

Surface temperatures have become warmer with increasing summer heat waves in the recent decades over most land areas, especially over Eurasia (Cohen et al., 2012; Hartmann et al., 2013; G. S. Jones et al., 2008; Seneviratne et al., 2014). Observational data show remarkably amplified warming trends during the summer over Europe-west Asia (EU) and East Asia (EA) but weak warming over Central Asia (CA) since the mid-1990s, indicating non-uniform decadal warming rates over Eurasia (Cohen et al., 2012; Hong et al., 2017). The rapid warming and increasing summer heat waves have serious impacts on human health, world's economies, and the environment, especially over densely populated Eurasia (IPCC, 2014). Thus, understanding the causes of these changes is very important and has attracted considerable attention.

The prevailing view is that the decadal to multidecadal climate variability over Eurasia was largely driven by the internal multidecadal variability of the climate system (i.e., Atlantic Multidecadal Oscillation [AMO]; Gao et al., 2019; Hong et al., 2017; Sun et al., 2019; Sutton & Dong, 2012; Sutton & Hodson, 2005). Changes in anthropogenic greenhouse gases (GHGs) and aerosols (Dong et al., 2016, 2017; Philipona et al., 2009; Ruckstuhl et al., 2008) may also contribute to the recent non-uniform warming pattern. However, their exact contributions to the summer non-uniform warming pattern over Eurasia remain elusive, as trend assessments are sensitive to the analysis time period and study area. For example, the trend assessments may not be true over shorter periods (e.g., from 1995 to 2012) when AMO's phase change may induce an apparent trend that is correlated with the anthropogenic forced trend (Schmidt et al., 2014). Furthermore, the recent AMO resulted from both internal climate variability and external forcing (Hua et al., 2019; Otterå et al., 2010; Qin et al., 2020a). Decadal variations in recent volcanic and anthropogenic aerosols forcing happen to be in phase with the internally generated AMO (Qin et al., 2020a, 2020b). Thus, the dominant factors regulating Eurasian multidecadal variations have not been clearly established. Understanding the contributions from the AMO and decadal variations in aerosol and other external forcing is, therefore, of great importance for near-term climate prediction and climate change adaption.

Here we use observations and a large number of Phase 6 of the Coupled Model Intercomparison Project (CMIP6; Eyring et al., 2016) model simulations to present evidence for a robust externally forced multidecadal surface air temperature (SAT) variations over EU (0°–50°E, 30–60°N) and EA (85°–120°E, 30°–60°N) during the June-July-August season. We used the multimodel ensemble mean (MMM) of the CMIP6 all-forcing (ALL) historical simulations as the estimated externally forced signal and removed it from observations to produce the residual fields that contain primarily internal variability (IV; see Section 2.2).

2. Data, Model Simulations, and Methods

2.1. Observational Data and Model Simulations

The primary monthly temperature data set used in this study is the Climatic Research Unit (CRU) TS v4.04 (Harris et al., 2020). To ensure the robustness of our results, we also tested three other global temperature data sets (Table S1), including the Berkeley Earth Surface Temperatures (Rohde et al., 2013), the Goddard Institute for Space Studies Surface Temperature Analysis version 4 (Lenssen et al., 2019) and the CRU Temperature version 4 (P. D. Jones et al., 2012).

The CMIP6 historical ALL (1850–2014) agents include time-varying GHGs, aerosols, ozone, solar irradiance (SI), and land use derived from observations. The effects of different historical external forcing agents were investigated by analyzing simulations (1850–2014) forced by GHG, NAT (natural forcing, solar plus volcanoes), anthropogenic aerosols (AA), volcanic aerosols (VA), SI and land-use forcing (Table S2). We also used the large ensembles of coupled climate model simulations from the Canadian Earth System Model version 2 (CanESM2; Hua et al., 2019; Kirchmeier-Young et al., 2017). These 50-member ensemble simulations were run with slightly different initial conditions and forced by historical ALL from 1950 to 2005 and with Representative Concentration Pathway forcing thereafter. In addition to the ALL forcing ensemble, we also analyzed two other 50-member ensembles of simulations with NAT and AA forcing.

2.2. Methods

We analyzed multiple temperature data sets over Eurasia (0°–80°N, 20°W–160°E) and focused on the 3-month period of June, July, and August. Additional regions of interest include EU, EA, and CA (55°–80°E, 35–55°N). We applied a low-pass filter (using a 19-point Lanczos filter with a 13-year cutoff period) to emphasize decadal to multidecadal variations in the observations and model simulations (Hua et al., 2018; Qin et al., 2020a).

The Silk Road Pattern (SRP; or the circum-global teleconnection) is a well-known teleconnection pattern over the Eurasian continent (Hong et al., 2017; Wang et al., 2017). The SRP index was defined as the principle component of the leading mode for 200 hPa meridional wind anomalies from the Twentieth Century Reanalysis version 3 (Slivinski et al., 2019) over Eurasia (20°–60°N, 0°–150°E). The AMO was defined as the low-pass filtered area-weighted average of the IV-induced sea surface temperatures (SST) over the North

Atlantic Ocean (80–0°W, 0°–60°N) as done previously (Qin et al., 2020a, 2020b). The Interdecadal Pacific Oscillation (IPO) index was defined following Hua et al. (2018).

2.2.1. Separating the Externally Forced and Internally Generated Components in the Observations

To estimate how much of the observed SAT variations over Eurasia may results from external forcing, we analyzed observations and model simulations following three steps. First, we used the global-mean SAT time series from the MMM of the CMIP6 ALL forcing historical simulations (from 1950 to 2014, 465 runs from 39 models; Table S2) as the forced signal and removed it through linear regression from the observed SAT at each grid point to produce the residual SAT fields that contain primarily unforced IV (Dai et al., 2015; Qin et al., 2020a, 2020b). Second, we removed the long-term linear trends from the observational SAT to emphasize the decadal to multidecadal variations (termed OBS*). The OBS* is a mix of externally forced and internally generated signals, that is, it represents the total multidecadal variations (i.e., due to both IV and external forcing) after removing its long-term linear trend. Third, we used the difference between the OBS* and IV to represent the externally forced component (EX, mainly from GHG and aerosols). In this way, we can separate the EX and IV components in the OBS*.

2.2.2. EOF and MCA Analysis

We performed an empirical orthogonal function (EOF) analysis of the SAT fields (i.e., OBS*, IV, EX, or single-forcing simulations by the CMIP6 models) to examine spatial and temporal characteristics of the leading modes over Eurasia. To identify the components in the OBS* whose temporal and spatial patterns are similar to those in the forced responses (i.e., CMIP6 MMM), we also performed maximum covariance analyses (MCA) of the observed and model-simulated multidecadal SAT fields.

2.2.3. Fingerprint Method

An optimal fingerprinting method was employed to compare observed and modeled SAT changes (Ribes et al., 2013). The observed changes Y are the linear sum of the responses to individual external forcings X (fingerprints) and the IV ε. For example, $Y = (X-\nu)\,\beta + \varepsilon$, where β represents the regression coefficient (also called scaling factor) and ν represents the sampling errors in fingerprints (i.e., the influence of IV in the modeled signal patterns). If the 90% confidence interval of β falls above 0, the corresponding modeled signals are considered to be detected in the observations. Fingerprints were estimated from the CMIP6 MMM for a given forcing (i.e., ALL or sum of GHG, AA, and NAT) and the IV was estimated from the fully coupled preindustrial control run from the CMIP6 models (455 non-overlapping 56-year segments from 39 models, similar to the temporal coverage of the observations from 1950 to 2005; we used the period from 1941 to 2014 and the first and last 9 years [1941–1949; 2006–2014] used mirrored data in the filtering, thus were less reliable and excluded). We conducted single-signal and three-signal analyses. For the former, observed changes were regressed onto the forced response to historical ALL forcing. For the latter, responses to GHG, AA, and NAT forcings were involved simultaneously in the regression. Using this method, one can examine whether the external signal is detectable in the observed changes. For example, the three-signal analysis was used to detect each signal influence in isolation, particularly aiming at quantifying the GHGs and aerosols to the observed changes. These regressions scale the model-simulated fingerprints to best fit the observations. Since the SAT responses to external forcing over EU and EA are spatially homogeneous, we used the regional average to increase the signal-to-noise ratio. More information on detection and attribution analysis can be found in previous studies (Allen & Stott, 2003; Ribes et al., 2013).

3. Results

3.1. Observed SAT Variations

Since SAT observations before about the 1950s are sparse over Eurasia (Figure S1), here we focus on the period since 1950. The SAT records show remarkable warming over the driest regions such as the Sahara Desert and the Arabian Peninsula (Zhou, 2016) and around Europe and Northeast Asia (Figure S2). Unlike observations, the rapid warming is more widespread across Eurasia in the CMIP6 ALL and GHG forcing-only simulations (Figure S2). Furthermore, the increases in global AA produce a cooling that offsets some of the GHG-induced warming in the ALL simulations (Figure S2).

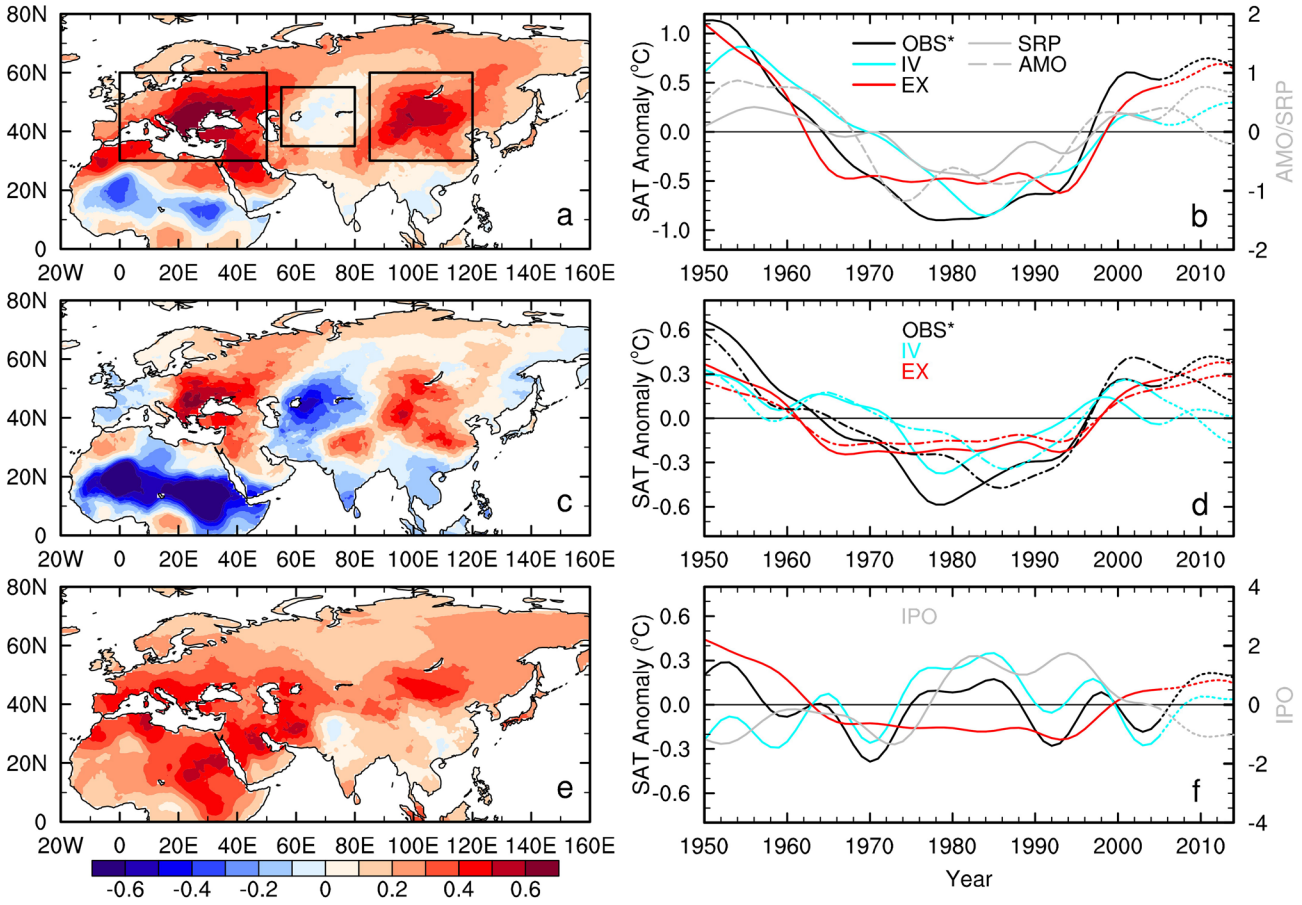

Figure 1. (a) Spatial patterns and (b) temporal variations (black line) of the leading empirical orthogonal function (61% variance) of the linearly detrended and smoothed June-July-August (JJA) surface air temperature (SAT; OBS*) from Climatic Research Unit TS v4.04 over Eurasia from 1950 to 2014. Also shown in (b) are the standardized, smoothed Atlantic Multidecadal Oscillation (gray dashed line) and the Silk Road Pattern indices (gray solid line). (c) Same as (a) but for the internal variability (IV) component in JJA SAT (44% variance), and its principal component (PC) is shown as the blue line in (b). (d) Regionally averaged time series of the smoothed JJA SAT anomalies (°C) from the OBS*, IV, and EX (externally forced component) over Europe-west Asia (EU, solid lines) and East Asia (EA, dashed lines). (e) Same as (a) but for the EX component (89% variance), and its PC is shown as the red line in (b). (f) Same as (d), but for Central Asia (CA). The outlined boxes in (a) represent the EU (0°–50°E, 30–60°N), CA (55°–80°E, 35–55°N), and EA (85°–120°E, 30°–60°N), respectively. Also shown in (f) is the standardized, smoothed Interdecadal Pacific Oscillation index (gray line). The last 9 years, plotted using dotted lines in (b, d, and f), used mirrored data in the filtering and thus are less reliable.

To focus on external forcing unrelated to the increasing trend in GHGs and AAs, we applied an EOF analysis of the linearly detrended, low-pass filtered SAT fields from the observations (hereafter termed OBS*) to quantify the spatial and temporal characteristics of the leading modes in Eurasian SAT. This allows us to focus on the decadal to multidecadal variations (without GHG-induced and aerosol-induced trends, see Section 2.2) in the SAT (Figure 1a).

The OBS* (black line in Figure 1b) shows large multidecadal variations over Eurasia, with negative anomalies from the mid-1960s to mid-1990s and positive anomalies in the 1950s and early 1960s and after the late 1990s. Large multidecadal warming (cooling) from about 1980 to 2014 (1950–1980) has occurred in EU and EA but with out-of-phase weak variations over CA (Figure 1a). Such a tripole pattern of multidecadal SAT variations is evident across other SAT data sets and is insensitive to the detrending methods applied (Figures S3 and S4).

3.2. Forced Versus Internal SAT Variations

The leading EOF of the low-pass filtered IV component estimated from the observations represents an internal tripole mode (Figure 1c) with multidecadal variations (Figure 1b), with a strong negative center in

CA (Figure 1c) whose temporal variations are highly correlated with the OBS* (Figure 1b). Previous studies (Hong et al., 2017; Gao et al., 2019; Sun et al., 2019) have linked the tripole pattern to the phase shift of the AMO around mid-1990s. The decadal to multidecadal changes in SST affect the regional climate over land via boundary forcing-induced atmospheric circulations (Sutton & Dong, 2012; Sutton & Hodson, 2005), and the AMO may contribute to the Eurasian non-uniform warming pattern through decadal changes in the SRP (Sun et al., 2019; Wang et al., 2017). Our analyses (Figures 1b and 1c) also suggest that the IV component of the multidecadal SAT variations over Eurasia is linked to the AMO. Furthermore, our results also show an association between the multidecadal SAT variations over CA and the IPO (Figure 1f; $r = 0.6$), which, however, should be interpreted with caution (Figure S1) due to limited gauges numbers compared to other two regions.

We estimate the externally forced component (EX, without trends) in observations as the difference between OBS* and IV at each grid box. The EX results mainly from the nonlinear components in GHGs and aerosols, and its leading EOF shows similar, AMO-like multidecadal variations (Figure 1b) but with the same sign for the spatial coefficients (Figure 1e). The combination of IV and EX components yields the tripole mode in the OBS*, with a weak center over CA (Figure 1a) that is mainly caused by the IV-induced negative center (Figure 1c). The regionally averaged SAT anomalies over EU and EA (Figure 1d) further confirm the EOF results, while the CA-mean SAT anomalies (Figure 1f) link the CA to the IPO. For the SAT anomalies (e.g., EX and IV) during the positive and negative phases, our estimates suggest that over EU (EA), approximately 61% (~56%) of the multidecadal SAT variations (i.e., OBS*) during 1950–2014 resulted from externally forced changes with the remaining coming from IV. In contrast, SAT variations over CA are mainly caused by IV component (e.g., IPO-like variability; Hua et al., 2018) that is roughly out of phase with the forced signal, leading to weak correlations there, although the forced signal does exist over CA. These results suggest that GHG, aerosols and other external forcing have caused detectable multidecadal changes in SAT over Eurasia.

Thus, the tripole SAT mode in observations (Figure 1a) is caused by both internal climate variability and external forcing. While the weak warming over CA is mainly caused by IV, more than half of the multidecadal SAT variations since 1950 over EU and EA result from external forcing, rather than mainly from IV as previously thought (Hong et al., 2017; Sutton & Dong, 2012; Sutton & Hodson, 2005).

To find out to what extent the observed warming pattern over Eurasia is forced by external forcing, we use the model-simulated SAT fields from the MMM of the CMIP6 ALL simulations as the forced signal, and performed a MCA of the MMM and the OBS* to extract the component in the OBS* that is associated with the forced mode in MMM (Figure 2). Clearly, the leading MCA mode of the MMM SAT accounts for most (~96%) of the smoothed SAT's spatiotemporal variations, whose temporal variations resemble those shown in Figure 1b. Associated with this forced mode, the MCA1 in the OBS* shows strong (weak) warming over EU and EA (CA) with the spatial pattern broadly consistent with that shown in Figure 1a (pattern correlation = 0.93). Although the OBS* contains unforced internal variations, nearly half (~48%) of the SAT spatiotemporal variations over Eurasia can be explained by the MCA1 that is associated with the externally forced mode (Figure 2). Thus, we conclude that multidecadal variations in external forcing may have contributed to nearly 50% of the non-uniform warming pattern over Eurasia since 1950.

3.3. Causes of the Forced Multidecadal Variations

To identify the key forcing agents of the multidecadal variations revealed by the MCA1 shown in Figure 2, we further analyze additional model simulations that were forced by different combinations of external forcing agents. AA and VA show multidecadal variations from 1950 to 2014; and the AA-forced SAT multidecadal variations exhibit a downward trend from 1950 to 1980 and an upward trend thereafter, contributing the most to the AMO-like variations in ALL simulations over EU and EA (Figure 3). Similarly, multidecadal variations in GHG (Figure S5), natural forcing (mainly VA) and other forcings also contribute to the multidecadal SAT variations over EU and EA (Figures 3 and S6). Thus, all the AA, GHG, and VA forcings may have contributed to the non-uniform multidecadal SAT variations over EU and EA since 1950, with AA contributing the largest (Figure S6).

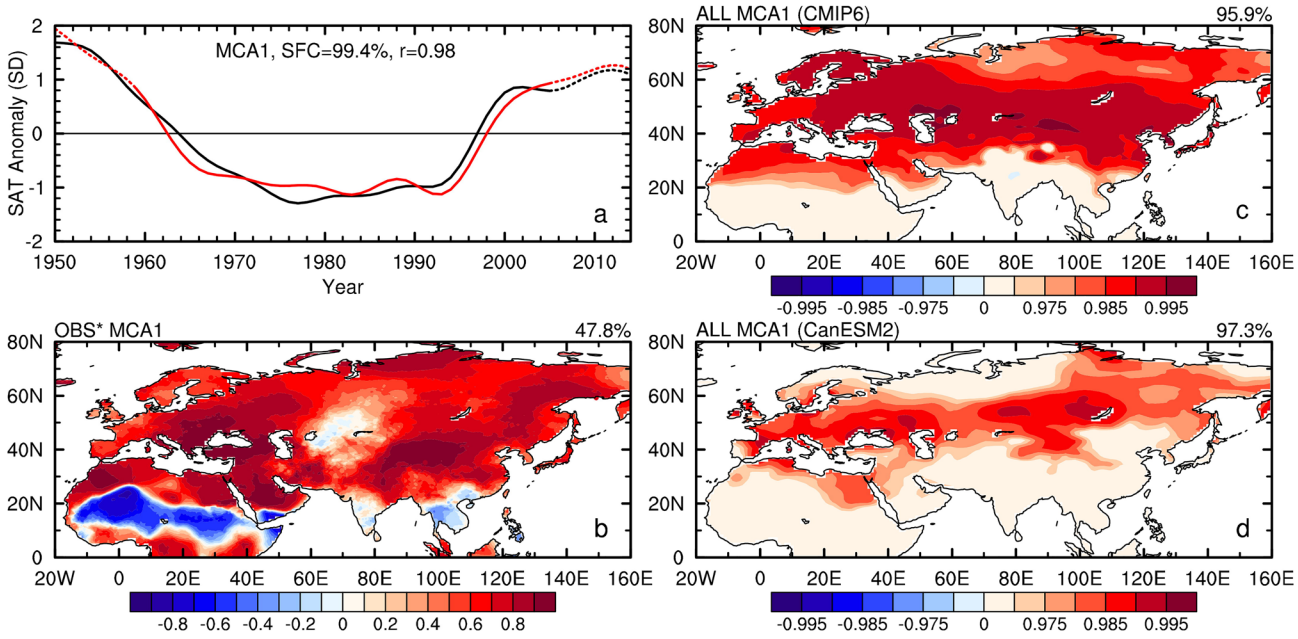

Figure 2. (a) Normalized temporal variations and (b)–(c) spatial patterns of the leading maximum covariance analyses (MCA) mode of the linearly detrended and smoothed surface air temperature from (b) Climatic Research Unit TS v4.04 (OBS*, black line) in (a) and (c) the Phase 6 of the Coupled Model Intercomparison Project (CMIP6) multimodel ensemble mean (red line in a) of the 465 all-forcing runs by 39 CMIP6 models from 1950 to 2014. Squared fractional covariance in (a) is the squared fractional covariance explained by the MCA mode and r is the correlation coefficient between the black and red lines in (a). (d) Same as (c), but for the ensemble mean of Canadian Earth System Model version 2 model simulations.

The leading EOF mode of the SAT fields from the AA forcing-only simulations exhibits pronounced multidecadal variations similar to the estimated EX component in the observations ($r = 0.97$, $p < 0.01$), especially over EU and the southwest of Lake Baikal (Figure S7). Such AA-forced non-uniform multidecadal SAT variations are also found in multidecadal anomaly composites (Figure S8). To verify whether these two regions may have been affected by historical aerosol forcing, we analyzed the SAT correlations between EU and EA on multidecadal time scales in a preindustrial control run and compared them with those from ALL and AA forcing runs by CanESM2 large ensemble simulations. The strong correlations between EU and EA seen in the historical ALL and AA forcing simulations disappear in the preindustrial control run that contains only IV (Figure S9). Thus, without external forcing, the strong correlation of the multidecadal SAT variations would disappear between these two regions and the AA forcing is a major contributor to the observed correlation.

Volcanic aerosols have also contributed to the multidecadal SAT variations in Eurasia (Figures 3 and S6). Recent volcanic eruptions, such as Agung in 1963, El Chichón in 1982 and Pinatubo in 1991, caused temporary cooling over Eurasia for a few years following the eruptions, especially around the Mediterranean Sea and the eastern Lake Balkhash (Figure S10). When smoothed using low-pass filtering, such temporary cooling results in multidecadal variations (Figure S11). The leading EOF mode of the linearly detrended and smoothed SAT fields from the VA forcing-only simulations exhibits multidecadal variations similar to the observed multidecadal signal ($r = 0.83$, $p < 0.05$; Figure S11), although the EOF does not show a tripole pattern as in observations. A volcanic influence on Eurasian SAT has been shown in paleoclimate data, with spatially synchronized variations over Europe and CA (Büntgen et al., 2016). Our results show that such VA-induced SAT variations also exist for recent volcanic eruptions. As a result, the AA- and VA-induced SAT variations are evident in the observations over EU and around EA. In particular, the SAT response to the AA forcing (Figures S7–S8) reveals a non-uniform pattern with the largest amplitude in EU and EA that contributes to the observed tripole pattern shown in Figure 1a, although the weak center over CA results mainly from IV (Figure 1c).

We conducted a formal detection and attribution analysis of the regional SAT changes over EU and EA in observations and CMIP6 simulations to estimate the contributions from individual forcing agents. Results

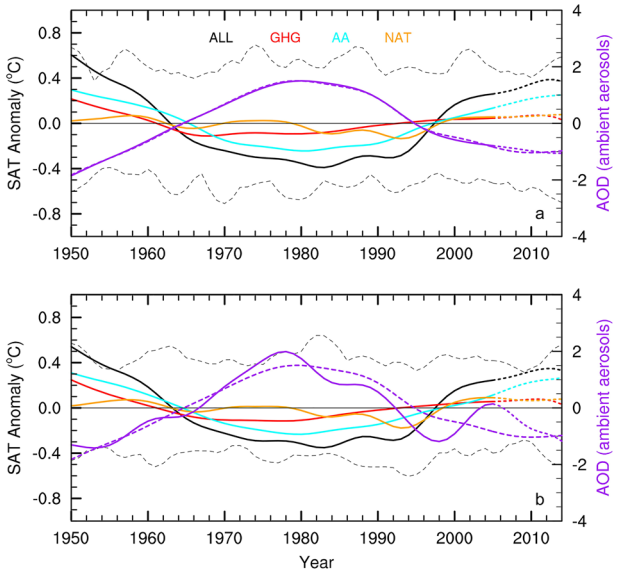

Figure 3. Time series of linearly detrended and smoothed June-July-August surface air temperature anomalies averaged over (a) Europe-west Asia and (b) East Asia from Phase 6 of the Coupled Model Intercomparison Project (CMIP6) multimodel ensemble mean (MMM) of the all-forcing (ALL, black) and single-forcing simulations with greenhouse gas (red), anthropogenic aerosols (AA; blue) and NAT (orange). The two gray dashed lines represent the ranges of the preindustrial control run. For the preindustrial control simulation, 455 non-overlapping segments from 39 models, similar to the length of the observations from 1950 to 2014, were used in estimating the IV-induced ranges. The purple solid lines in (a) and (b) represent the normalized time series of the linearly detrended and smoothed ambient aerosol optical depth (AOD) at $\lambda = 550$ nm averaged over Europe-west Asia and East Asia from the AA forcing-only simulations, respectively. The purple dashed line represents the time series of the principal component of the leading empirical orthogonal function mode in the linearly detrended and smoothed ambient AOD over Eurasia from the MMM of the CMIP6 AA forcing simulations from 1950 to 2014. The results (i.e., PC1) are similar when using the global AOD fields.

from one-signal detection analysis show that the ALL (i.e., sum of GHG, AA, and NAT) signal is detected (Figure S12). However, the models overestimate (i.e., with a scaling factor smaller than unity) the SAT variations over EA, while slightly underestimate the SAT variations over EU. Previous studies have indicated that there is less agreement between climate models and observations in terms of the magnitudes and spatial patterns associated with multidecadal variability (Kravtsov, 2017; Parsons et al., 2020; Power et al., 2017). The causes of the observations versus model discrepancies at decadal to multidecadal time scales need further investigation.

To explore whether the detected external influence can be separated into GHG, AA, and NAT contributions, we conducted a three-signal analysis (Figure 4). Over EA, GHG, and NAT signals are detectable in separation from AA's influences, although the GHG signal has a large uncertainty range for the scaling factor. Over EU, AA's influences are robustly detected with the 5%–95% range of the scaling factor lying above zero, consistent with significant multidecadal SAT variations in the observations and AA forcing-only simulations. Previous studies (Qin et al., 2020a, 2020b) have shown that aerosol forcing could contribute to AMO-like North Atlantic SST variations. Our new finding suggests that the AMO-like multidecadal SAT variations around EU are dominated by the AA forcing.

4. Summary and Discussion

We have analyzed observations and ALL and single-forcing historical simulations by 39 CMIP6 models to show that more than half of the multidecadal SAT variations from 1950 to 2014 over EU and EA have resulted from external forcing (i.e., GHG and aerosols). In contrast, the recent SAT over CA is influenced mainly by internal decadal variations in the Atlantic and Pacific Oceans.

Our results suggest that both external forcing and IV contributed to the non-uniform pattern of the SAT changes from 1950 to 2014. However, the possible mechanisms for the influence of the external forcing on the non-uniform pattern need further investigation. For example, the GHG-induced multidecadal SAT variations exhibit regional features (Figure S5; e.g., due to warming amplification over the driest regions around West Asia; Zhou, 2016). In addition, AA have changed greatly in magnitude, composition and geographical locations since the early twentieth century (Smith & Bond, 2014; Xie et al., 2013), especially over EU and EA (Qin et al., 2020b). The aerosol forcing and its climate response are more localized than GHG forcing, which can lead to different SAT change patterns, such as strong (weak) anomalies over Europe and EA (CA; Figures S7 and S8). The aerosol optical depth over Eurasia tracks the regional SAT well (Figure 3). On the other hand, AA over EA have started to decline in recent years due to controls on air pollution (Li et al., 2016), which may cause less cooling over EA since the 2000s (Figure 1d). Thus, the combinations of GHG and aerosols could lead to strong warming (cooling) from about 1980 to 2014 (1950–1980) around EU and EA, but relatively weak warming (cooling) over CA, contributing to the non-uniform pattern over Eurasia from 1950 to 2014.

Given the large externally forced influence on Eurasian SAT variations, it may be possible to improve the decadal prediction of Eurasian SAT for the coming decades with estimated near-future changes in GHGs and aerosols. However, this will depend on how well the state-of-the-art models simulate the response to a given AA and GHG forcing and how well we can project these forcings for the upcoming decades. Nevertheless, improved understanding of the internally generated and externally forced climate variations is constructive for regional climate prediction. Looking ahead into the coming decades, AA will continue to

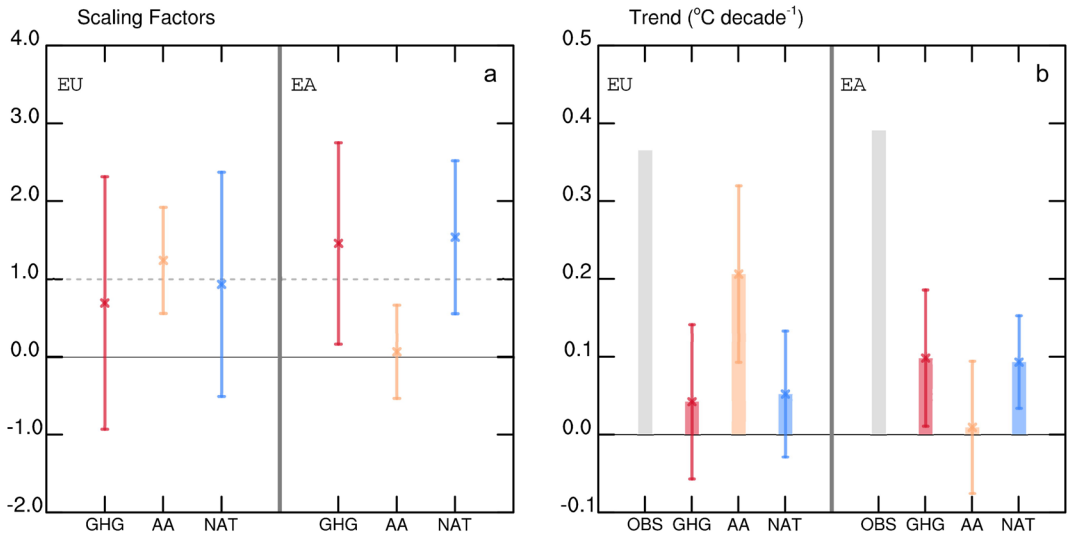

Figure 4. Results from optimal fingerprinting analysis. (a) Best estimates (cross points) and 5%–95% uncertainty ranges (error bars) of the scaling factors (β) from the three-signal (greenhouse gas [GHG], anthropogenic aerosols [AA], and NAT) analyses of the linearly detrended and smoothed June-July-August surface air temperature (SAT) averaged over Europe-west Asia (EU) and East Asia (EA) from 1950 to 2005. (b) Observed trend (gray) and attributed trends to GHG (red), AA (orange), and NAT (blue) forcing from 1980 to 2005. The attributed trend is estimated as the linear trends of the relevant time series multiplied by corresponding scaling factors. The 1980–2005 period was chosen because year 1980 is the time when the observed SAT started to increase.

decrease, whereas the AMO will likely be in its positive phase. These factors, together with continued increases in GHGs, will likely further accelerate warm-season hot temperatures over EU and EA.

Data Availability Statement

The CanESM2 large ensembles were downloaded from http://crd-data-donnees-rdc.ec.gc.ca/CCCMA/products/CanSISE/output/CCCma/CanESM2/. CRU TS v4.04 data was downloaded from https://crudata.uea.ac.uk/cru/data/hrg/cru_ts_4.04/. BEST data was downloaded from http://berkeleyearth.org/data/. GISTEMP v4 data was downloaded from https://psl.noaa.gov/data/gridded/data.gistemp.html. CRUTEM4 data was downloaded from https://psl.noaa.gov/data/gridded/data.crutem4.html.

Acknowledgments
This work was supported by the National Natural Science Foundation of China (42088101, 42075022 and 41625019) and the National Natural Science Foundation of Jiangsu Province (BK20200096). A. Dai was supported by the National Science Foundation (grant nos. AGS-2015780 and OISE-1743738) and the U.S. National Oceanic and Atmospheric Administration (grant no. NA18OAR4310425). L. Zhou was supported by National Science Foundation (grant nos. AGS-1952745). The authors acknowledge the World Climate Research Programme, which, through its Working Group on Coupled Modeling, coordinated and promoted CMIP6. The authors thank the climate modeling groups for producing and making available their model output, the Earth System Grid Federation (ESGF) for archiving the data and providing access, and the multiple funding agencies who support CMIP6 and ESGF (https://esgf-node.llnl.gov/projects/cmip6/).

References

Allen, M. R., & Stott, P. A. (2003). Estimating signal amplitudes in optimal fingerprinting, Part I: Theory. *Climate Dynamics*, *21*, 477–491. https://doi.org/10.1007/s00382-003-0313-9

Büntgen, U., Myglan, V. S., Ljungqvist, F. C., McCormick, M., Di Cosmo, N., Sigl, M., et al. (2016). Cooling and societal change during the Late Antique Little Ice Age from 536 to around 660 AD. *Nature Geoscience*, *9*, 231–236. https://doi.org/10.1038/ngeo2652

Cohen, J. L., Furtado, J. C., Barlow, M., Alexeev, V. A., & Cherry, J. E. (2012). Asymmetric seasonal temperature trends. *Geophysical Research Letters*, *39*, L04705. https://doi.org/10.1029/2011GL050582

Dai, A., Fyfe, J. C., Xie, S.-P., & Dai, X. (2015). Decadal modulation of global surface temperature by internal climate variability. *Nature Climate Change*, *5*, 555–559. https://doi.org/10.1038/nclimate2605

Dong, B., Sutton, R. T., Chen, W., Liu, X., Lu, R., & Sun, Y. (2016). Abrupt summer warming and changes in temperature extremes over Northeast Asia since the mid-1990s: Drivers and physical processes. *Advances in Atmospheric Sciences*, *33*, 1005–1023. https://doi.org/10.1007/s00376-016-5247-3

Dong, B., Sutton, R. T., & Shaffrey, L. (2017). Understanding the rapid summer warming and changes in temperature extremes since the mid-1990s over Western Europe. *Climate Dynamics*, *48*, 1537–1554. https://doi.org/10.1007/s00382-016-3158-8

Eyring, V., Bony, S., Meehl, G. A., Senior, C. A., Stevens, B., Stouffer, R. J., & Taylor, K. E. (2016). Overview of the Coupled Model Intercomparison Project Phase 6 (CMIP6) experimental design and organization. *Geoscientific Model Development*, *9*, 1937, 19581958. https://doi.org/10.5194/gmd-9-1937-2016

Gao, M., Yang, J., Gong, D., Shi, P., Han, Z., & Kim, S.-J. (2019). Footprints of Atlantic Multidecadal Oscillation in the low-frequency variation of extreme high temperature in the Northern Hemisphere. *Journal of Climate*, *32*, 791–802. https://doi.org/10.1175/JCLI-D-18-0446.1

Harris, I., Osborn, T. J., Jones, P., & Lister, D. (2020). Version 4 of the CRU TS monthly high-resolution gridded multivariate climate dataset. *Scientific Data*, *7*, 109. https://doi.org/10.1038/s41597-020-0453-3

Hartmann, D. L., Klein Tank, A. M. G., Rusticucci, M., Alexander, L. V., Brönnimann, S., Charabi, Y., et al. (2013). Observations: Atmosphere and Surface. In T. F. Stocker, D. Qin, G.-K. Plattner, M. Tignor, S. K. Allen, J. Boschung, et al. (Eds.), *Climate Change 2013: The Physical Science Basis* (pp. 159–254). Cambridge University Press.

Hong, X., Lu, R., & Li, S. (2017). Amplified summer warming in Europe-West Asia and Northeast Asia after the mid-1990s. *Environmental Research Letters*, *12*, 094007. https://doi.org/10.1088/1748-9326/aa7909

Hua, W., Dai, A., & Qin, M. (2018). Contributions of internal variability and external forcing to the recent Pacific decadal variations. *Geophysical Research Letters*, *45*, 7084–7092. https://doi.org/10.1029/2018GL079033

Hua, W., Dai, A., Zhou, L., Qin, M., & Chen, H. (2019). An externally-forced decadal rainfall seesaw pattern over the Sahel and southeast Amazon. *Geophysical Research Letters*, *46*, 923–932. https://doi.org/10.1029/2018GL081406

IPCC. (2014). Climate Change 2014: Impacts, Adaptation, and Vulnerability. In C. B. Field, V. R. Barros, D. J. Dokken, K. J. Mach, M. D. Mastrandrea, & T. E. Bilir (Eds.), *Part A: Global and Sectoral Aspects*. Cambridge University Press.

Jones, G. S., Stott, P. A., & Christidis, N. (2008). Human contribution to rapidly increasing frequency of very warm Northern Hemisphere summers. *Journal of Geophysical Research*, *113*, D02109. https://doi.org/10.1029/2007JD008914

Jones, P. D., Lister, D. H., Osborn, T. J., Harpham, C., Salmon, M., & Morice, C. P. (2012). Hemispheric and large-scale land surface air temperature variations: An extensive revision and an update to 2010. *Journal of Geophysical Research*, *117*, D05127. https://doi.org/10.1029/2011JD017139

Kirchmeier-Young, M. C., Zwiers, F. W., & Gillett, N. P. (2017). Attribution of extreme events in Arctic Sea ice extent. *Journal of Climate*, *30*, 553–571. https://doi.org/10.1175/JCLI-D-16-0412.1

Kravtsov, S. (2017). Pronounced differences between observed and CMIP5-simulated multidecadal climate variability in the twentieth century. *Geophysical Research Letters*, *44*, 5749–5757. https://doi.org/10.1002/2017GL074016

Lenssen, N. J. L., Schmidt, G. A., Hansen, J. E., Menne, M. J., Persin, A., Ruedy, R., & Zyss, D. (2019). Improvements in the GISTEMP uncertainty model. *Journal of Geophysical Research: Atmospheres*, *124*, 6307–6326. https://doi.org/10.1029/2018JD029522

Li, Z., Lau, W. K.-M., Ramanathan, V., Wu, G., Ding, Y., Manoj, M. G., et al. (2016). Aerosol and monsoon climate interactions over Asia. *Reviews of Geophysics*, *54*, 866–929. https://doi.org/10.1002/2015RG000500

Otterå, O. H., Bentsen, M., Drange, H., & Suo, L. (2010). External forcing as a metronome for Atlantic multidecadal variability. *Nature Geoscience*, *3*, 688–694. https://doi.org/10.1038/ngeo955

Parsons, L. A., Brennan, M. K., Wills, R. C. J., & Proistosescu, C. (2020). Magnitudes and spatial patterns of interdecadal temperature variability in CMIP6. *Geophysical Research Letters*, *47*, e2019GL086588. https://doi.org/10.1029/2019GL086588

Philipona, R., Behrens, K., & Ruckstuhl, C. (2009). How declining aerosols and rising greenhouse gases forced rapid warming in Europe since the 1980s. *Geophysical Research Letters*, *36*, L02806. https://doi.org/10.1029/2008GL036350

Power, S., Delage, F., Wang, G., Smith, I., & Kociuba, G. (2017). Apparent limitations in the ability of CMIP5 climate models to simulate recent multi-decadal change in surface temperature: Implications for global temperature projections. *Climate Dynamics*, *49*, 53–69. https://doi.org/10.1007/s00382-016-3326-x

Qin, M., Dai, A., & Hua, W. (2020a). Quantifying contributions of internal variability and external forcing to Atlantic multidecadal variability since 1870. *Geophysical Research Letters*, *47*, e2020GL089504. https://doi.org/10.1029/2020GL089504

Qin, M., Dai, A., & Hua, W. (2020b). Aerosol-forced multidecadal variations across all ocean basins in models and observations since 1920. *Science Advances*, *6*, eabb0425. https://doi.org/10.1126/sciadv.abb0425

Ribes, A., Planton, S., & Terray, L. (2013). Application of regularized optimal fingerprinting to attribution. Part I: Method, properties and idealized analysis. *Climate Dynamics*, *41*, 2817–2836. https://doi.org/10.1007/s00382-013-1735-7

Rohde, R., Muller, R. A., Jacobsen, R., Muller, E., Perlmutter, S., Rosenfeld, A., et al. (2013). A new estimate of the average Earth surface land temperature spanning 1753 to 2011. *Geoinformatics & Geostatistics: An Overview*, *1*, 1. https://doi.org/10.4172/2327-4581.1000101

Ruckstuhl, C., Philipona, R., Behrens, K., Collaud Coen, M., Dürr, B., Heimo, A., et al. (2008). Aerosol and cloud effects on solar brightening and the recent rapid warming. *Geophysical Research Letters*, *35*, L12708. https://doi.org/10.1029/2008GL034228

Schmidt, G. A., Shindell, D. T., & Tsigaridis, K. (2014). Reconciling warming trends. *Nature Geoscience*, *7*, 158–160. https://doi.org/10.1038/ngeo2105

Seneviratne, S. I., Donat, M. G., Mueller, B., & Alexander, L. V. (2014). No pause in the increase of hot temperature extremes. *Nature Climate Change*, *4*, 161–163. https://doi.org/10.1038/nclimate2145

Slivinski, L. C., Compo, G. P., Whitaker, J. S., Sardeshmukh, P. D., Giese, B. S., McColl, C., et al. (2019). Toward a more reliable historical reanalysis: Improvements for version 3 of the Twentieth Century Reanalysis system. *Quarterly Journal of the Royal Meteorological Society*, *145*, 2876–2908. https://doi.org/10.1002/qj.3598

Smith, S. J., & Bond, T. C. (2014). Two hundred fifty years of aerosols and climate: The end of the age of aerosols. *Atmospheric Chemistry and Physics*, *14*, 537–549. https://doi.org/10.5194/acp-14-537-2014

Sun, X., Li, S., Hong, X., & Lu, R. (2019). Simulated influence of the Atlantic Multidecadal Oscillation on summer Eurasian nonuniform warming since the mid-1990s. *Advances in Atmospheric Sciences*, *36*, 811–822. https://doi.org/10.1007/s00376-019-8169-z

Sutton, R. T., & Dong, B. (2012). Atlantic Ocean influence on a shift in European climate in the 1990s. *Nature Geoscience*, *5*, 788–792. https://doi.org/10.1038/ngeo1595

Sutton, R. T., & Hodson, D. L. R. (2005). Atlantic Ocean forcing of North American and European summer climate. *Science*, *309*, 115–118. https://doi.org/10.1126/science.1109496

Wang, L., Xu, P., Chen, W., & Liu, Y. (2017). Interdecadal variations of the Silk Road pattern. *Journal of Climate*, *30*, 9915–9932. https://doi.org/10.1175/JCLI-D-17-0340.1

Xie, S.-P., Lu, B., & Xiang, B. (2013). Similar spatial patterns of climate responses to aerosol and greenhouse gas changes. *Nature Geoscience*, *6*, 828–832. https://doi.org/10.1038/ngeo1931

Zhou, L. (2016). Desert amplification in a warming climate. *Scientific Reports*, *6*, 31065. https://doi.org/10.1038/srep31065